Biochemistry **2007,** *46,* 11639−11649

Protein Dynamics and Monomer−Monomer Interactions in AntR Activation by Electron Paramagnetic Resonance and Double Electron−Electron Resonance[†]

K. Ilker Sen,[‡,§] Timothy M. Logan,[‡,§,||] and Piotr G. Fajer*,[‡,§,⊥]

Institute of Molecular Biophysics, Department of Chemistry and Biochemistry, and Department of Biological Sciences,
Florida State University, Tallahassee, Florida 32306, and National High Magnetic Field Laboratory,
1800 East Paul Dirac Drive, Tallahassee, Florida 32310

Received May 7, 2007; Revised Manuscript Received July 31, 2007

ABSTRACT: The Anthracis repressor (AntR) is a Mn(II)-activated DNA binding protein that is involved in the regulation of Mn(II) homeostasis in *Bacillus anthracis*. AntR is structurally and functionally homologous to Mn(II)-activated repressor from *Bacillus subtillis* (MntR). Our studies on AntR focus on metal-regulated activation of the protein. Line shape analysis of continuous wave electron paramagnetic resonance (EPR) spectra showed that metal binding resulted in a general reduction of backbone dynamics and that there were no further changes in backbone motion upon DNA binding. Double electron−electron resonance (DEER) pulsed EPR spectroscopy was used to measure distances between nitroxide spin labels strategically placed in dimeric AntR. The DEER data were analyzed assuming Gaussian distributions for discrete populations of spins. A structural model for AntR was built from homology to MntR, and the experimentally measured distances were simulated to distinguish between spin label and backbone motions. Together with the computational analysis, the DEER results for apo-AntR indicated relatively narrow conformational distributions for backbone residues at the dimer interface and near the metal binding site. No significant changes were observed on these sites in the presence of metal or DNA. On the other hand, the distribution of the conformers and the distances between the putative DNA binding helices decreased upon metal binding. These results suggest that the DNA binding region of AntR shows large amplitude backbone motions in the absence of metal, which may preclude sequence-specific binding to promoter sites. Metal binding narrows the range of conformations accessible in this region and shortens the mean distance between the DNA binding helices, probably resulting in alignment that optimizes promoter recognition and binding.

The diphtheria toxin repressor (DtxR)[1] proteins regulate metal ion homeostasis in a wide range of bacterial species (*1*−*3*). These proteins generally regulate multiple genes simultaneously, coordinating the expression of metal ion transporters, metal storage proteins, and proteins involved in metal capture and sequestration by the bacterium (*4*−*6*). In addition to the metal homeostasis function, DtxR-like proteins also regulate the expression of virulence gene products (*6*). Therefore, defining the molecular mechanisms associated with metal-induced activation of these proteins is of particular interest.

The DtxR family of proteins can be divided into two subfamilies based on the number of domains. The larger subfamily, represented by DtxR from *Corynebacterium diphtheria* and the iron-dependent regulator (IdeR) from *Mycobacterium tuberculosis*, contains two domains. The N-terminal domain provides residues for metal binding, DNA binding, and a dimer interface (*7*−*9*). The C-terminal domain appears to regulate repressor activation through effects on dimer dissociation energetics in the apo-form of the repressor and by metal coordination in the holo-repressor (*10*). The smaller size subfamily, which includes manganese transport regulator (MntR) from *Bacillus subtillis* and Anthracis repressor (AntR) from *Bacillus anthracis*, contains a single domain which is structurally homologous to the N-terminal domain of DtxR, including conservation of the metal-coordinating residues (*11*, *12*). The single-domain subfamily proteins lack the C-terminal domain but contain an extended dimer interface.

The current model of a metal activation mechanism for the two-domain subfamily includes structural transition from a disordered to an ordered state of the N domain. In the absence of metal, these proteins exist in a partially folded, weakly dimeric state (*13*). Metal-induced ordering increases the affinity to form dimers (*14*) and locks the DNA binding helices into an optimal conformation for binding double-stranded DNA, resulting in an active repressor.

[†] Supported by grants from the National Science Foundation (MCB 0346650 to P.G.F.), National Institutes of Health (R01 AI021628 to T.M.L.), Florida State University Research Foundation (P.G.F.), and a predoctoral fellowship of the American Heart Association−Florida−Puerto Rico Affiliate to K.I.S.

* To whom correspondence should be addressed. Tel: 850-645-1337. Fax: 850-644-7244. E-mail: fajer@magnet.fsu.edu.

[‡] Institute of Molecular Biophysics, Florida State University.

[§] National High Magnetic Field Laboratory.

[||] Department of Chemistry and Biochemistry, Florida State University.

[⊥] Department of Biological Sciences, Florida State University.

[1] Abbreviations: AntR, Mn(II)-activated repressor from *Bacillus anthracis*; DtxR, diphtheria toxin repressor; IdeR, iron-dependent repressor from *Mycobacterium tuberculosis*; MntR, Mn(II)-activated repressor from *Bacillus subtillis*; EPR, electron paramagnetic resonance.

10.1021/bi700859p CCC: $37.00

Metal activation in single-domain members of the DtxR family is less well-understood. Cooperative metal binding, similar to that seen in DtxR and IdeR, has been observed for MntR and AntR (*15*, *16*). However, the metal binding site in MntR is fundamentally different from what is seen in DtxR or IdeR: The selectivity is toward Mn(II) rather than Fe(II), and the metals are separated by 4.4 Å rather than 9 Å (*17*). Furthermore, MntR and AntR are dimeric in the absence of metal (*15*, *16*), and metal binding does not appreciably alter the fraction of dimer formed.

Given the similarities in overall structure between the MntR and the N domain of DtxR and IdeR, the differences in metal binding and dimer affinity are intriguing. In this study, we investigated possible activation scenarios for AntR. Because AntR is already present as a dimer in the absence of the bound metal, dimerization cannot play a significant role in the activation pathway. Instead, metal binding must induce some kind of structural or dynamical change in the conformation of the protein, which activates the repressor. Structural rearrangement of protein segments is likely due to different geometries in the apo and holo structures of the MntR protein (*18*). Here, we used site-directed spin labeling (*19*) and double electron−electron resonance (DEER) pulsed electron paramagnetic resonance (EPR) spectroscopy to measure distances and conformational distributions between spin-labeled sites in dimeric AntR. Measured distances in spin-labeled proteins include the length of the label side chain and the distribution of distances due to spin label rotamers. We distinguished the backbone and spin label contributions to experimental distance distributions by molecular modeling of the spin label rotamers.

Changes in protein dynamics upon metal binding were proposed previously for DtxR's N-terminal domain (*14*) and, given its sequence homology to AntR, it is likely that the conformational dynamics plays a role during metal activation. Continuous wave (cw) EPR spectroscopy, which is sensitive to side chain and backbone dynamics in the nanosecond range, was used to investigate conformational dynamics in AntR in the presence and absence of Mn(II) ions. Three spin labeling sites were chosen to report on the nature of the extended dimer interface, on the metal binding sites, and on the DNA binding helices.

The results of this study indicate that AntR is less flexible in the metal bound state than the apo-state. Metal binding has relatively minor effects on the overall structure, except in the DNA binding region. Surprisingly, DNA binding had no further affects on conformational flexibility beyond what was induced by metal binding alone. These results provide insights into the metal activation of the single-domain members of the DtxR family.

MATERIALS AND METHODS

Protein Expression, Purification, and Spin Labeling. Wild-type AntR does not contain a native cysteine. Single Cys mutants for spin labeling were prepared using the QuikChange kit (Stratagene). Primers used in mutagenesis were 5′-TTAGTGTACATCCATGCTCTGTAACAAAAATGG-TGCAAAAA and 5′-TTTTTGCACCATTTTTGTTACA-GAGCATGGATGTACACTAA for S37C, 5′-TTATATT-GAACAAATTTATTGTTTGATTGATGAAAA and 5′-TTTTCATCAATCAAACAATAAATTTGTTCAAT-ATAA for L15C, and 5′-AATACTTTGAACAAGATTGT-GTTCGAGTGGAAA and 5′-TTTCCACTCGAACACAAT-CTTGTTCAAAGTATT for E124C, all purchased from Integrated DNA Technologies, Inc. Expression and purification were performed as described in ref *16*, except that after the protein was clarified, 20 mM DTT was added together with EDTA, followed by dialysis and desalting as in the previously reported protocol. All buffers used in the subsequent steps were degassed and Chelex (Bio-Rad Inc.) treated. Protein yields for each Cys mutant were similar to wild-type AntR (100−160 mg/L). Labeling with N-(1-oxy-2,2,6,6-tetramethyl-4-piperidinyl)iodoacetemide (IASL), N-(1-oxy-2,2,5,5-tetramethyl-4-piperidinyl)maleimide (MSL), and 1-oxyl-2,2,5,5-tertramethyl-δ_3-pyrroline-3-(methyl)methanethiosulfonate (MTSSL) spin labels was carried out by incubation overnight at room temperature (298 K) at 4-fold molar excess of spin label over 500 μM AntR monomer in 10 mM HEPES and 500 mM NaCl, pH 7.0. Unreacted label was removed by exhaustive dialysis at 4 °C against 4 L of the same buffer, with three changes in 4−6 h intervals. The efficiency of labeling was calculated from the spin concentration determined from the second integral of EPR spectra using spin label solutions of known concentration and from protein concentration determined by UV absorption at 276 nm using predicted extinction coefficients of 18450 M^{-1} cm^{-1} (*16*). All samples were labeled to 0.90−0.98 labels/protein.

Mobility Shift Assays. For electrophoretic mobility shift assays of spin-labeled AntR complexed with its cognate DNA, BAmntHO strand (200 nm) (*20*) and spin-labeled apo-AntR (20 μM) were mixed, allowed to stand for 10 min at room temperature, and loaded on 6% polyacrylamide gel in 40 mM Tris borate buffer, pH 7.0. $MnCl_2$ (200 μM) was added to sample, gel, and running buffers immediately prior to electrophoresis. Gels were stained with ethidium bromide, illuminated with UV light (FBTI-88, Fisher Scientific, PA), and photographed with an electrophoresis system camera (FB-PDC-34, Fisher Scientific).

EPR Spectroscopy. Cw EPR spectra were recorded at room temperature (298 K) using a Bruker EMX series spectrometer (Bruker Biospin, Billerica, MA) equipped with a TE_{102} rectangular cavity. Samples were sealed in 50 μL glass capillaries (VWR International, PA). For metal-activated AntR, the protein was incubated with $ZnSO_4$ at a 4:1 Zn(II) to protein molar ratio, and for DNA-bound repressor, AntR was incubated with target DNA at a 1:1 molar ratio. Instrumental parameters for cw experiments were as follows: 9.6 GHz microwave frequency, 2 mW microwave power, 1 G modulation amplitude, 100 kHz modulation frequency, 41 ms conversion time, 41 ms time constant, and 1024 points acquisition within 100 or 120 G field sweep. Spectral line shapes were simulated with a Monte Carlo/SIMPLEX algorithm incorporating the stochastic Liouville equation (*21*). Magnetic g and A tensors were determined from spectral analysis of AntR immobilized by reaction with diisothiocyanate (DITC) glass beads (Sigma-Aldrich, St. Louis, MO), which eliminate the global motion of the protein and result in line shapes determined by magnetic tensors without any motional averaging due to global motion (*22*−*25*).

For DEER experiments, spin-labeled AntR mutants were transferred into protein buffer containing 30% ethylene glycol for glass formation, which provides a homogeneous distribution of proteins and prevents phase separation induced by crystallization of water during freezing. Samples (100 μL) in 4 mm O.D. 3.2 mm I.D. quartz capillaries were fast frozen by dipping into liquid nitrogen immediately before inserting into the precooled resonator. Pulsed EPR spectra were recorded on a Bruker Elexys 680 spectrometer equipped with a Bruker dielectric ring resonator (model MD-5). In the 4-pulse DEER experiment (*17*), the frequency of the pump pulse was adjusted to the resonator dip and the static field was set to the low-field resonance of the nitroxide signal. To minimize the orientation selection and maximize the fraction of coupled spins (and thus signal-to-noise), the observed pulse was applied at 65 MHz upfield from the pump frequency. This arrangement observes the spins at the low field resonance while pumping the spins at the center of the spectrum. Typical $\pi/2$ pulse lengths were 16 ns, and the echo was integrated using an integration window equal to the echo width. Data were analyzed using home-written MATLAB software, which assumes a sum of Gaussian-distributed conformers contributing to the observed echo modulation. The program employs the Monte Carlo/SIMPLEX algorithm to find the distance distribution resulting in the dipolar evolution function that best describes the experimental data (*26*). Selection of the number of Gaussian populations used to describe the experimental data is based on a statistical F test. The software is available at http://fajerpc.magnet.fsu.edu.

Conformational Modeling of Spin Label Side Chains in AntR. Simulations were performed with CHARMM (*27*) using the CHARMM19 extended atom force fields with a distance-dependent dielectric constant and topologies as described in ref *28*. A detailed description of the methods and the scripts used for modeling is available at http://fajerpc.magnet.fsu.edu. AntR's structure was homology built (*29*) from the structure of Mn(II)-bound MntR [pdb code: 1ON1 (*12*)] and energy minimized. Residues 15, 37, and 124 were mutated in silico to spin label side chains using the Biopolymer module of Insight II 2000 (Molecular Simulations Inc.). The modeling was divided into two stages. First, conformational space accessible to a spin label in a specific location of AntR was searched by a Metropolis Monte Carlo minimization (MMCM) algorithm (*30*, *31*). An initial structure for the docked spin label was chosen arbitrarily, and for each iteration, a randomly chosen dihedral angle in the spin label side chain was rotated by a random amount. This conformer was then energy minimized while the entire protein structure was restrained ("rigid cage assumption"). The generated structure was accepted if it had lower potential energy than the previously accepted structure. If not, the Metropolis criterion (*32*) was applied at 300 K to determine whether to accept or reject the structure. For each spin label, 1500−2000 minimized structures were generated to exhaustively survey the rotamer space. The 300 lowest energy conformers were selected for each AntR monomer, and the structures of the dimers were reconstructed by calculating all possible combinations for the low energy conformers. The distances between various spin labels across the AntR dimer were measured from these structures using a home written MATLAB program where the probability for a given interspin distance was calculated assuming a Boltzmann distribution in the total energies of the conformers (*30*, *31*).

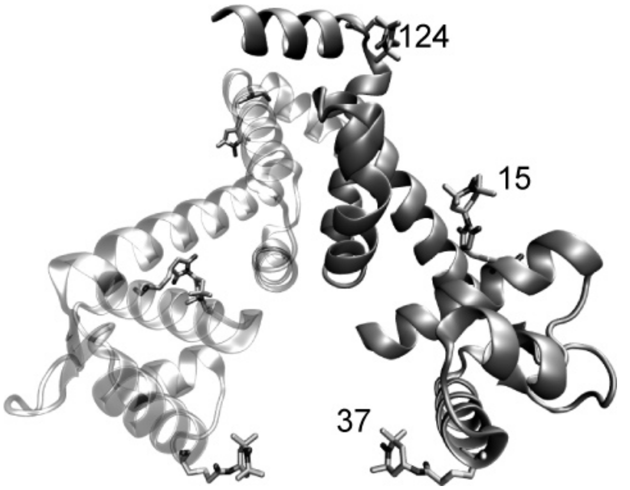

FIGURE 1: Mutation sites with attached spin labels on a homology-built AntR dimer structure. Sites L15, S37, and E124 were mutated to cysteine and modified with spin labels IASL, MSL, and MTSSL.

To relieve the rigid cage assumption and to sample the local environment of the found minima, we used molecular dynamics (MD). The MD trajectory was calculated using the lowest energy conformers from the MMCM calculation as seeds (*28*). All atoms within a 15 Å radius of the spin label were allowed to move in the MD trajectory. The protein was slowly heated (12 ps simulation with 2 fs time steps) to 300 K and equilibrated for 200 ps with 1 fs time steps. The production run was performed for 2−4 ns with 2 fs time steps. The interspin distances extracted from individual trajectories were pooled using home-written scripts for VMD software package (*28*, *33*).

RESULTS

Homology Modeling and Mutagenesis. The three sites on AntR for spin labeling were selected on the basis of great similarity with MntR (84% sequence identity). The X-ray structure of Mn(II)-bound MntR [pdb code: 1ON1 (*12*)] was used as a template, and AntR was homology modeled (*29*). Residue L15, close to the metal binding sites (Figure 1), residue S37, in the DNA binding domain, and residue E124, located on a helix at the dimer interface, were selected for cysteine mutagenesis to facilitate spin labeling. The possibility of functional perturbation by mutagenesis and spin labeling was assayed by binding of each spin-labeled mutant to the cognate DNA (electrophoretic mobility shift assay, Figure 2). AntR mutants labeled at sites L15C and E124C bound fully to DNA; however, site S37C showed reduced binding (40−60% of wild type), probably due to its proximity to the DNA binding site.

Dynamics of AntR. The changes in the local environment of the nitroxide spin label attached to the cysteine side chain in the rotational correlation time range of 0.1−100 ns (*34*) are reflected in the line shapes of resonances in the cw EPR spectrum. The vantage points for AntR spin labeling were chosen to report on dynamic properties of the DNA binding helix (S37C), the dimer interface (E124C), and the metal binding site (L15C). Figure 3 illustrates the EPR spectra and spectral simulations of MTSSL- and MSL-labeled AntR-(E124C). The best fit parameters from the spectral line shape simulations are given in Table 1. The spectra were simulated with two components having the same g and A tensors but

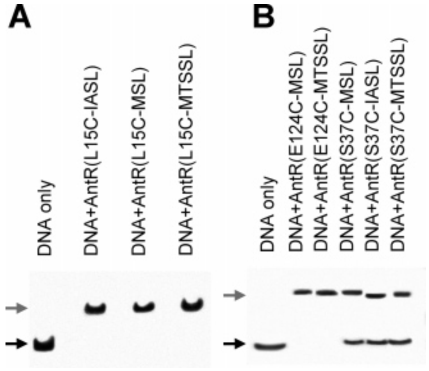

FIGURE 2: DNA shift assay gels, showing a double-stranded DNA target of AntR (black arrow) and a complex of DNA and AntR protein (gray arrow). (A) Binding comparison of spin-labeled L15C mutants, all showing full binding; (B) full binding of spin-labeled E124C and partial binding of S37C-labeled mutants.

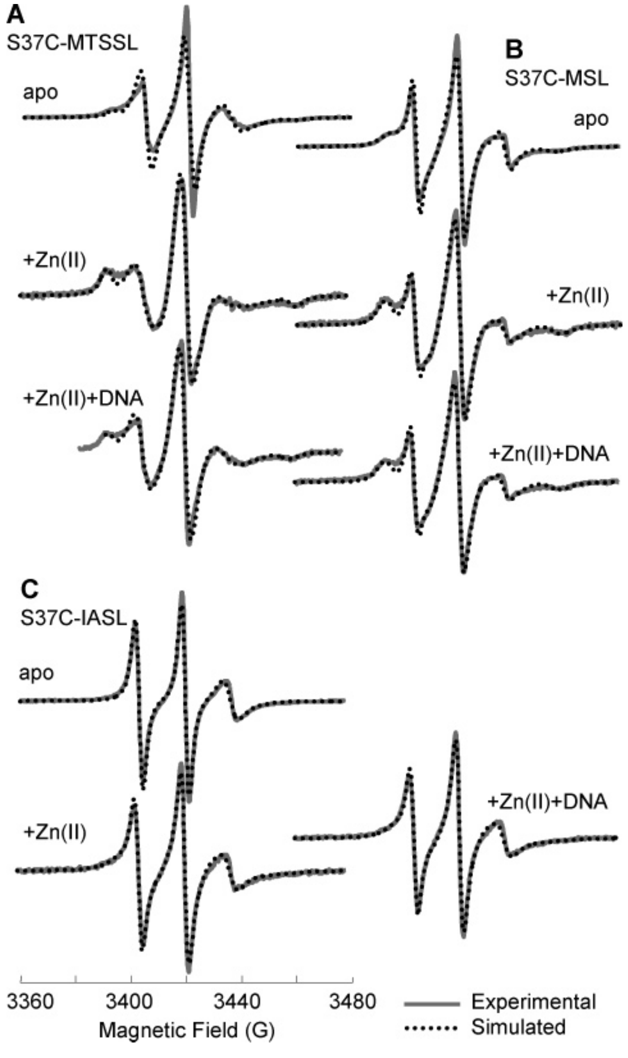

FIGURE 3: EPR spectra (solid gray) and line shape simulations (dotted black) of MTSSL- (A) and MSL- (B) labeled AntR(E124C) in apo, Zn(II) bound, and Zn(II) and DNA bound states.

different motions parametrized with rotational correlation time (τ_R), which is derived from the diffusion tensor components (R in Table 1). The diffusion rate tensor is anisotropic ($R_{xx} \neq R_{yy} \neq R_{zz}$); however, there is no preferential motion about any principal axis of the magnetic tensor among the analyzed spectra. The simulated line shapes for all spectra in this study were least sensitive to changes in R_{zz}. The value R_{zz} was randomly distributed in Monte Carlo fittings between the boundaries (0.1 and 167 ns). This is because the spectral resolution in the central feature of the spectrum is low, where the magnetic tensor components g_{xx}, g_{yy}, g_{zz}, A_{xx}, and A_{yy} overlap with each other. For ease of comparison, we report the average rotational correlation time τ_{av} calculated from R_{xx} and R_{yy} (Table 1 legend).

EPR spectra of MSL-labeled AntR(E124C) recorded in the absence of metal (apo), with bound Zn(II), and in presence of metal and DNA are shown in Figure 3B. In the absence of Zn(II) ions, the spectrum of apo-AntR exhibits two populations that differ in the time scale of motion and fractional contributions: The less-populated faster motion (25%) results in narrow spectral line shapes and more abundant (75%) slower motion by broader spectral line shapes observed in the "wings" of the spectrum. The corresponding rotational correlation times obtained from line shape analysis are $\tau_{av} = 0.8 \pm 0.2$ ns and $\tau_{av} = 4.0 \pm 1.9$ ns for the two populations in the apoprotein. As shown in Figure 3B, the spectrum of Zn(II)-bound AntR also demonstrates a similar sharp feature, but the slower component is even broader, suggesting a decrease in the mobility. When Zn(II) is introduced to the sample, the fast component remains unchanged at $\tau_{av} = 0.8 \pm 0.4$ ns; however, the second correlation time increases to $\tau_{av} = 6.5 \pm 1.5$ ns, suggesting a decrease of dynamics in AntR's structure with metal binding. DNA binding does not change the motion further (Figure 3B and Table 1).

The MTSSL label at site E124C exhibited features alike to those described for AntR(E124C-MSL), in both the apo- and the metal-bound repressors (Figure 3A and Table 1). Similar spectral changes were observed for all spin labels at L15C and S37C as well (Figures 4 and 5 and Table 1). It appears that metal binding induces a loss of backbone flexibility in the holo-repressor relative to the apo-repressor in at least three different regions on the protein. DNA binding induces no further changes in protein dynamics.

Intermonomer Distances Measured Using DEER EPR Spectroscopy. To investigate possible changes of monomer rearrangement upon metal activation, we measured the strength of dipolar interspin interactions in dimeric AntR. The distances between the monomers were determined using the same sites used to probe the conformational dynamics (L15C, S37C, and E124C). Because the interspin distances are anticipated to be greater than 1.8 nm and the dipolar broadening of already broad cw spectra is small and difficult to extract (*35*), we used a pulsed EPR technique, DEER. The dipolar evolution signal is the modulation of the spin echo as the timing of the pumping pulse is swept between the two π-pulses at the observation frequency (*36*). The dipolar echo evolution signals of 4-pulse DEER experiments of spin-labeled apo- and metal-bound AntR mutants as well as the Gaussian population analysis are shown in Figures 6−9 for the three sites.

The dipolar evolution in Figure 6 (top row) demonstrates a fast initial decay, which is indicative of a strong dipolar interaction, corresponding to a distance of 1.8−2.5 nm. The persistence of the oscillations suggests that the distribution of distances is relatively narrow; broad (>1.5 nm) distributions, such as are seen for S37C mutants (Figure 8), dampen the oscillations entirely. To quantitatively describe the distribution of distances that give rise to such a dipolar

Table 1: Simulation Parameters of Spin-Labeled AntR Mutants' Spectra[a]

site and label	state	R_{xx}	R_{yy}	τ_{av}	ratio[b] (%)	g_{xx}	g_{yy}	g_{zz}	A_{xx}	A_{yy}	A_{zz}	w_{xx}	w_{yy}	w_{zz}	gib0
124 MSL	Apo	8.3 ± .1	8.3 ± .1	0.8 ± .2	28.0	a	b	c	7.0	7.0	37.5	0.6	0.1	0.5	1.3
		7.3 ± .2	7.8 ± .2	4.0 ± 1.9	72.0	“	“	“	“	“	37.5	0.1	1.8	0.1	2.6
	Zn	8.3 ± .1	8.3 ± .3	0.8 ± .4	23.8	“	“	“	“	“	36.9	“	1.4	“	1.3
		7.7 ± .1	6.0 ± .1	6.5 ± 1.5	76.2	“	“	“	“	“	35.5	“	0.1	“	2.5
	DNA	8.4 ± .5	8.3 ± .4	0.7 ± .9	24.0	“	“	“	“	“	36.9	“	1.4	“	1.3
		7.7 ± .1	6.0 ± .1	6.5 ± 1.5	76.0	“	“	“	“	“	35.5	“	0.1	“	2.5
124 MTSSL	Apo	7.5 ± .1	8.1 ± .1	2.1 ± .5	49.6	d	e	f	6.0	6.0	35.0	0.5	0.5	0.5	1.3
		6.7 ± .1	8.0 ± .1	3.2 ± .7	50.4	“	“	“	7.0	“	“	“	“	“	“
	Zn	6.0 ± .2	6.0 ± .2	167 ± 79	13.0	“	“	“	“	“	“	1.0	1.0	1.0	2.5
		7.2 ± .1	7.9 ± .2	3.5 ± 1.5	87.0	“	“	“	“	“	“	0.6	0.6	0.6	1.3
	DNA	6.0 ± .3	6.0 ± .2	167 ± 101	8.9	“	“	“	“	“	“	1.0	1.0	1.0	2.5
		7.3 ± .1	7.9 ± .1	3.4 ± .8	91.1	“	“	“	“	“	“	0.6	0.6	0.6	1.3
15 MSL	Apo	7.1 ± .1	8.4 ± .1	1.3 ± .3	40.8	a	b	c	7.0	7.0	36.0		0.3	“	“
		7.2 ± .1	7.4 ± .2	8.1 ± 3.1	59.2	“	“	“	“	“	35.5	0.6	“	“	
	Zn	8.2 ± .3	7.4 ± .2	1.8 ± 1.3	21.0	“	“	“	“	“	36.0	“	“	“	
		7.3 ± .1	7.2 ± .1	9.3 ± 2.2	79.0	“	“	“	“	“	35.5	“	“	“	
	DNA	9.5 ± 1	7.4 ± .3	0.1 ± .5	18.2	“	“	“	“	“	36.0	1.0	1.0	1.0	“
		6.0 ± .1	6.0 ± .1	167 ± 39	91.8	“	“	“	“	“	35.5	0.6	0.6	0.6	“
15 MTSSL	Apo	8.1 ± .1	7.6 ± .1	2.0 ± .5	66.2	d	e	f	6.0	6.0	35.0	0.2	0.2	0.2	1.0
		6.0 ± .1	8.1 ± .2	2.6 ± 1.2	33.8	“	“	“	7.0	“	“	“	“	“	1.1
	Zn	7.9 ± .2	7.5 ± .1	3.0 ± 1.2	87.7	“	“	“	6.0	“	“	0.6	0.6	0.6	1.3
		6.0 ± .1	7.8 ± .3	5.2 ± 3.8	12.3	“	“	“	7.0	“	“	“	“	“	“
	DNA	6.0 ± .1	7.9 ± .1	4.1 ± 1	66.7	“	“	“	6.0	“	“	“	“	“	“
		8.0 ± .1	8.0 ± .1	1.7 ± .4	33.3	“	“	“	“	“	“	“	“	“	“
37 MSL	Apo	7.8 ± .1	8.4 ± .2	1.1 ± .4	34.0	a	b	c	6.5	8.5	35.5	“	“	“	“
		6.4 ± .2	7.7 ± .1	6.3 ± 1.5	66.0	“	“	“	“	7.5	35.3	“	“	“	2.5
	Zn	7.1 ± .2	8.3 ± .2	1.6 ± .7	32.1	“	“	“	“	“	36.0	“	“	“	1.3
		6.2 ± .4	7.4 ± .1	12.5 ± 3.4	67.9	“	“	“	“	“	35.3	“	0.5	0.5	3.0
	DNA	7.2 ± .1	8.3 ± .2	1.5 ± .7	34.2	“	“	“	“	“	36.0	“	0.6	0.6	1.3
		7.4 ± .1	6.2 ± .4	12.5 ± 3.4	65.8	“	“	“	“	“	35.3	“	0.5	0.5	3.0
37 MTSSL	Apo	6.7 ± .4	6.6 ± .3	37.1 ± 34	28.7	d	e	f	7.0	6.0	35.0	“	0.6	0.6	1.3
		8.0 ± .1	7.7 ± .1	2.2 ± .5	71.3	“	“	“	“	“	“	“	“	“	“
	Zn	6.0 ± .1	6.3 ± .3	111 ± 61	52.1	“	“	“	“	“	“	1.6	1.6	1.6	2.2
		7.3 ± .1	8.0 ± .1	2.8 ± .6	47.9	“	“	“	6.0	“	“	0.6	0.6	0.6	1.3
	DNA	6.0 ± .1	6.8 ± .3	45.6 ± 30	45.7	“	“	“	7.0	“	“	1.6	1.6	1.6	2.5
		6.9 ± .2	8.3 ± .4	1.6 ± 1.6	54.3	“	“	“	6.0	5.0	“	0.6	0.6	0.6	1.3
37 IASL	Apo	8.3 ± .2	7.5 ± .1	1.4 ± .6	45.3	a	g	h	7.5	7.7	35.7	“	0.1	0.1	“
	Zn	8.2 ± .2	7.5 ± .1	1.8 ± .8	54.7	“	“	“	“	“	“	“	“	“	“
		7.2 ± .1	7.8 ± .1	4.2 ± 1	45.7	“	“	“	“	“	“	2.9	0.7	1.6	2.9
	DNA	8.2 ± .2	7.5 ± .1	1.8 ± .8	54.3	“	“	“	“	“	“	0.6	0.1	0.1	1.3
		7.2 ± .1	7.8 ± .1	4.2 ± 1	45.3	“	“	“	“	“	“	2.9	0.7	1.6	1.1

[a] Values that are same as the previous row are denoted with ‘‘. w and gib_0 are the Lorentzian and Gaussian line widths; R is the log of rotational diffusion rate constant in s^{-1}; τ_{av} is the average rotational correlation time, which is calculated from $\tau_{av} = 1/3(10^{R_{xx}} + 10^{R_{yy}})$; and ratio % is the percentage contribution of a population to the overall intensity. [b] The estimated error in ratios from Monte Carlo searches is less than 10% for all samples. For simplification, the following symbols were used instead of *g* values: a = 2.009 ± 0.0006, b = 2.007 ± 0.0001, c = 2.0029 ± 0.0001, d = 2.0078 ± 0.0007, e = 2.0065 ± 0.0008, f = 2.0025 ± 0.0002, g = 2.0056 ± 0.0006, and h = 2.0021 ± 0.0002 (the errors correspond to those of DITC-bound AntR spectra simulations; see Figure S1).

evolution decay curve, we fitted the experimental data with the simulated dipolar evolution expected for a sum of Gaussian distributions of distances. Each Gaussian population is characterized by their own mean distance (r), width (Δ), and amplitude. The number of individual Gaussians and parameters describing each Gaussian that best model the dipolar evolution decay was determined by a Simplex fitting procedure and a statistical F test to ensure that the decay curves were not overdetermined (*26*). The resulting best fits are shown in the left panel of Figure 6 overlaid on the experimental dipolar evolution. The corresponding distance distributions are shown in the center panel. The uniqueness of the solution and the associated errors are determined from the goodness of fit (χ^2) surface shown in the right panel of Figure 6. The χ^2 surface around the best solution is created by random sampling of all of the distance parameters for each Gaussian population that result in the fits better than $\chi_{\mathrm{best}}^2 + 1$. The width of the χ^2 contour reflects the error with which the best solution is determined at 68% confidence. The narrow contour implies a well-defined solution; parameters outside this region result in bad fits ($\chi^2 > 1 + \chi_{\mathrm{best}}^2$). The uniqueness of a given solution is identified by the absence of multiple minima in the χ^2 surface. When a given solution optimizes to give a broad width for a Gaussian, with corresponding shallow χ^2 surfaces, this solution is referred to as "poorly defined". For example, in Figure 6, the MTSSL-labeled site 124 has a well-defined distance distribution composed of a single Gaussian having the most probable distance, $r = 3.0 \pm 0.2$ nm, and width, $\Delta = 0.5 \pm 0.5$ nm. However, in the presence of Zn(II), a second population appears with a longer distance ($r = 4.2 \pm 0.7$ nm) but with a significantly less well-determined width ($\Delta = 1.7 \pm 2.8$ nm).

The major advantage of this quantitative analysis of the DEER echo decay curves is that it allows us to investigate conformational changes associated with metal and DNA

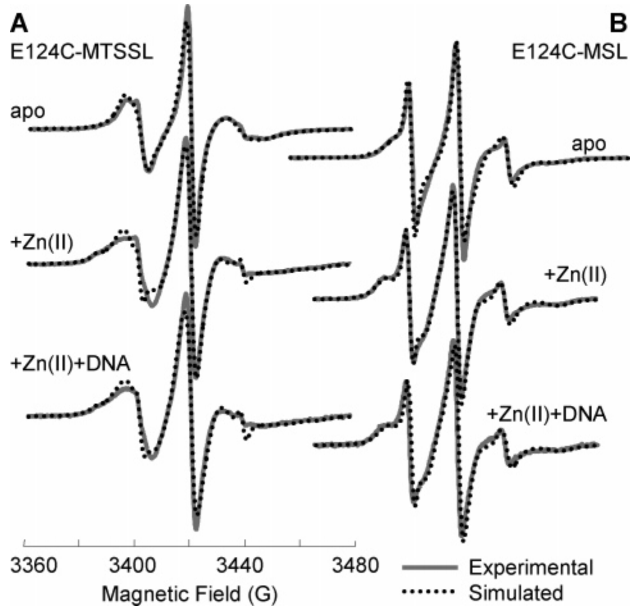

FIGURE 4: EPR spectra (solid gray) and line shape simulations (dotted black) of MTSSL- (A) and MSL- (B) labeled AntR(L15C) in apo, Zn(II) bound, and Zn(II) and DNA bound states.

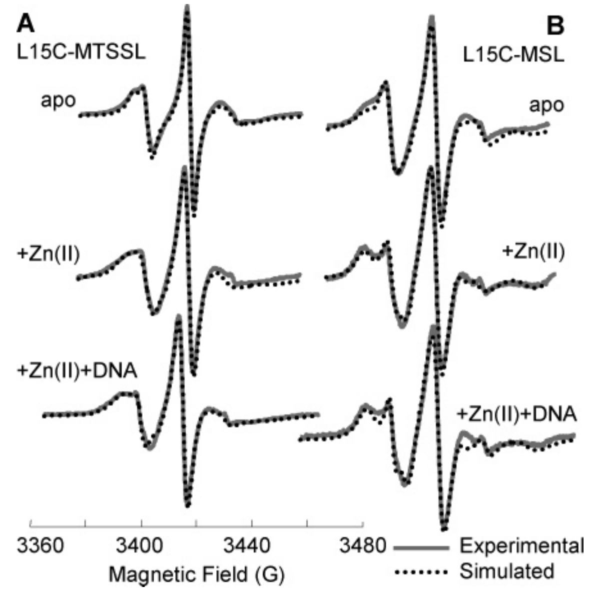

FIGURE 5: EPR spectra (solid gray) and line shape simulations (dotted black) of MTSSL- (A), MSL- (B), and IASL- (C) labeled AntR(E124C) in apo, Zn(II) bound, and Zn(II) and DNA bound states.

binding at three sites in AntR and to assign statistical weights to the data interpretation.

Dimer Interface (E124C). There are no significant differences between MSL- and MTSSL-labeled AntR124C distance distributions in either the apo- or the Zn(II)-bound states (Figure 6). With the exception of the MTSSL-labeled apo sample, two Gaussian populations were necessary to reproduce the dipolar evolution. The main population (77−100% mole fraction) was well-defined (with a sharp minimum in the error surfaces), centered around a distance of 3 nm with a width of 0.75 nm. A second, minor conformer (11−23% mole fraction) was characterized by longer mean distances ($r > 4$ nm) with broad width (2.5 nm). The small differences in the DEER traces between the apo and the Zn-bound states are due to changes to that second population.

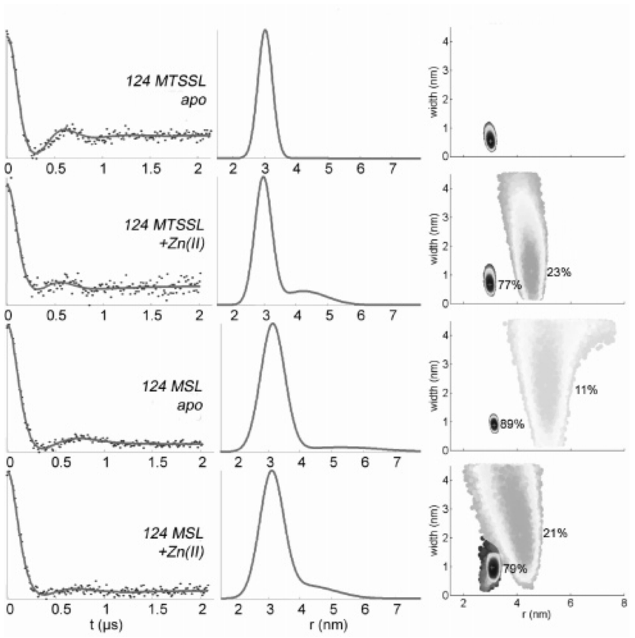

FIGURE 6: Distances between the monomers of MTSSL- and MSL-labeled AntR(E124C) in the presence and absence of Zn(II). Dipolar evolution (left panel, points), best fits (solid line) corresponding to distance distributions in the center panel, and χ^2 surfaces (right panel) are shown, and the fraction of each population is displayed next to the χ^2 contours.

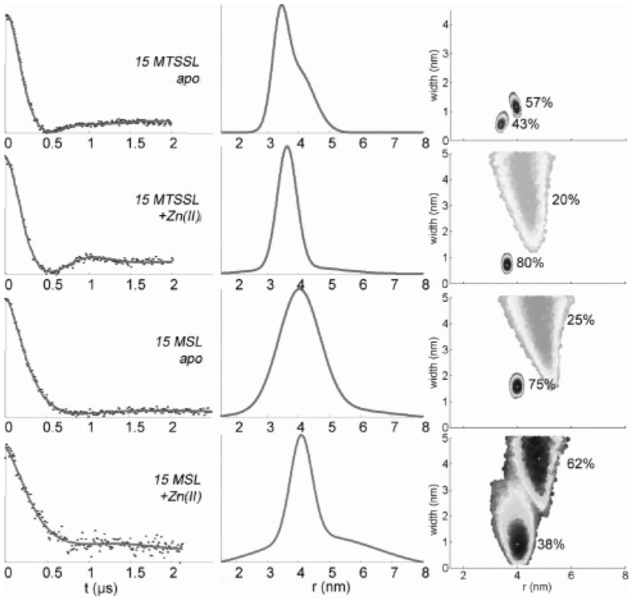

FIGURE 7: Distances between the monomers of MTSSL- and MSL-labeled AntR(L15C) in the presence and absence of Zn(II). Dipolar evolution (left panel, points), best fits (solid line) corresponding to distance distributions in the center panel, and χ^2 surfaces (right panel) are shown. The fraction of each population is displayed next to the χ^2 contours.

The molecular basis for this minor conformation is unclear. For instance, it might arise from a minor fraction of denatured protein or from an additional dimer conformer in the apo state (this is unlikely to be an explanation in the metal-bound repressor, though). This minor distribution is also poorly defined, as shown by broad, shallow minima in the χ^2 surfaces. Given this, we focus on the major population. The center of this population differed very slightly between the spin labels ($r_1 = 3.0 \pm 0.3$ nm for MTSSL and 3.1 ±

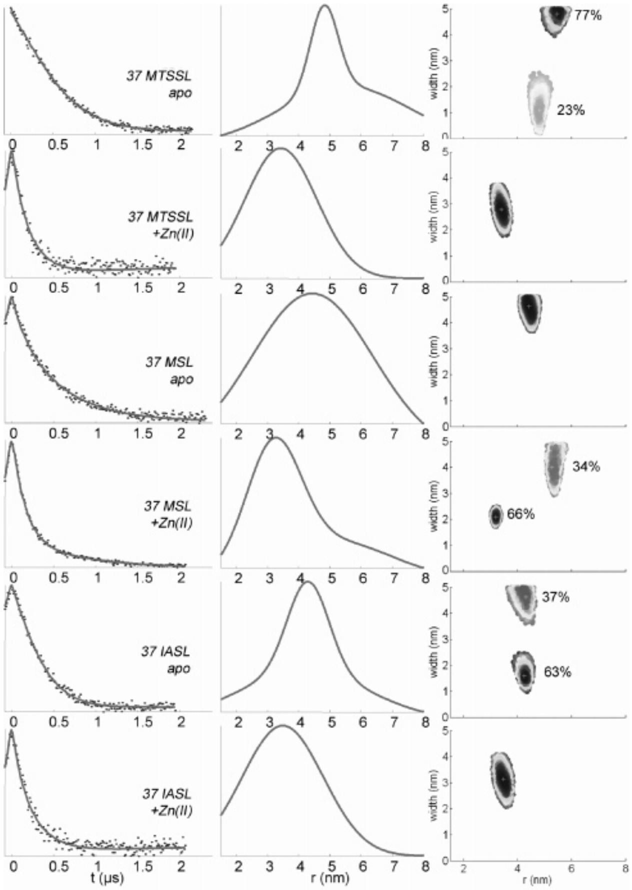

FIGURE 8: Distances between the monomers of MTSSL-, MSL-, and IASL-labeled AntR(S37C) in the presence and absence of Zn(II). Dipolar evolution (left panel, points), best fits (solid line) corresponding to distance distributions in the center panel, and χ^2 surface (right panel) are shown. The fraction of each population is displayed next to the χ^2 contours.

0.3 nm for MSL). The distance between the N−O bond and the C_β can be as much as 9.1 and 7.7 nm for MTSSL and MSL, respectively. Therefore, the minor difference is easily rationalized by the different structures of the spin labels rather than in the protein backbone. The width of the distance distribution, Δ, was more varied, 0.5 ± 0.6 nm for MTSSL and 0.9 ± 0.6 for MSL. Again, the larger size of MSL implies a larger surface covered by possible rotamers and hence a larger width of distance distribution.

Metal Binding Region (L15C). The dipolar evolution of the MSL and MTSSL spin labels at L15C was described by two Gaussian populations. These two populations are most clearly defined for MTSSL in the apo protein, where the most probable distance and the width of the distributions are well-defined, with approximately equivalent populations. Interestingly, the MSL spin label also shows two populations with most probable distances roughly the same as for MTSSL, but here, the major conformer adopts a shorter distance while the longer distance is poorly defined. Because MSL has a larger molecular volume than the MTSSL side chain (vida supra), it is possible that the second conformer corresponds to a pocket on the protein that can accept MTSSL but not MSL.

Comparison of apo and holo states of the protein revealed no major change in mean distances induced by Zn(II) binding: The major distance (r_1) was 3.4 ± 0.2 nm in the apo state and 3.6 ± 0.2 nm for the holo state of MTSSL-labeled protein, and for the MSL-labeled protein, r_1 was 4.0 ± 0.3 and 4.1 ± 0.5 nm for apo and holo states, respectively. Widths of the populations were not significantly different (Table 2). As with site 124, the second broad populations on site 15 were associated with large errors (±0.8 to ± 2.3 nm for r_2 and ±1.9 to ±3.2 for Δ_2). As for site 124, the differences in DEER traces are also ascribable to this second population. The mean distance of the first population is 0.5−0.6 nm shorter for MTSSL ($r_1 = 3.4 \pm 0.2$ nm for apo and 3.6 ± 0.2 nm for holo) than for MSL ($r_1 = 4.0 \pm 0.3$ nm for apo and 4.1 ± 0.5 nm for holo). As it will be discussed later in the manuscript, this is most likely due to different conformer orientations of these labels, since modeling of the spin labels on this site shows similar difference in the distances (Figure 10). A distorted backbone conformation in one of the samples is also a possible cause for the difference in distances between spin labels, although it is unlikely since both samples are fully capable of DNA binding (Figure 2).

DNA Binding Region (S37C). Residue S37 is in the DNA binding helix−turn−helix motif of AntR. Therefore, structural changes induced by metal binding in this region may be most directly related to the activation pathway of AntR. In the absence of metal, the intermonomer distances range from 4.2 ± 1.1 to 5.5 ± 1.1 nm (Figure 8 and Table 2). Unlike the other two sites (124 and 37), the distance distribution between the monomers is very broad: $\Delta_1 = 4.6 \pm 1.1$ to 5.0 ± 1.1 nm for the major population. A surface-exposed residue such as site 37 (Figure 1), which is not restricted by nearby residues or tertiary interactions, is expected to have a large distance distribution due to the flexibility of the spin label side chain. The distance between C_β and the N−O bond for each spin label in a completely extended conformation is as much as 8.7, 9.1, and 7.7 nm for IASL, MSL, and MTSSL, respectively. Therefore, in the cases where the spin labels are facing toward or away from each other on the same protein, the width of the distance distribution may be as much as four times the spin label tether length (3.5, 3.6, and 3.1 nm for IASL, MSL, and MTSSL, respectively). Experimentally, the widths seen in the distance distbutions are larger than this (4.6 ± 1.1 to 5.0 ± 1.1 nm) and must be due to multiple backbone conformations.

In the presence of Zn(II), the distances shorten by ∼1 nm to 3.4 ± 0.4, 3.2 ± 0.2, and 3.5 ± 0.4 nm for MTSSL-, MSL-, and IASL-labeled AntR(S37C), respectively, and the widths of distributions narrow significantly ($\Delta = 2.7 \pm 1.1$, 2.1 ± 0.5, and 3.1 ± 1.1 nm for MTSSL, MSL, and IASL). DNA binding did not induce further changes in distances (Figure 9).

Changes in Dimerization. Another parameter that is derived from the DEER experiments is *f*, the fraction of coupled spins having an interaction distance of 1.8 to ∼7 nm. The larger is this fraction, the deeper is the modulation depth (M_D), which is the ratio of echo modulation to the overall echo intensity. In AntR samples, the increase or decrease in M_D values was between 12.4 and 24.0% upon binding of metal (Table 2). Furthermore, all *f* values were less than 1, suggesting a lack of higher molecular weight aggregates or of an oligomerization state higher than a dimer, consistent with the observation that AntR is predominantly dimeric, as reported previously (*16*).

Table 2: Distance Distribution from DEER Experiments[a]

site	label	state	M_D (%)	f	r_1 (nm)	Δ_1 (nm)	%	r_2 (nm)	Δ_2 (nm)	%	$F_{1\to2}$	$F_{2\to3}$	$P_{1\to2}$	$P_{2\to3}$
124	MTSSL	apo	17.9 ± 0.8	0.63	3.0 ± 0.2	0.5 ± 0.5	100				1.13	-	0.21	-
124	MTSSL	Zn	17.2 ± 1.0	0.60	3.0 ± 0.3	0.6 ± 0.6	77	4.2 ± 0.7	1.7 ± 2.8	23	1.36	0.98	0.02	0.55
124	MSL	apo	14.6 ± 0.2	0.50	3.1 ± 0.2	0.9 ± 0.4	89	5.3 ± 1.0	3.0 ± 2.5	11	3.50	0.98	0.00	0.54
124	MSL	Zn	15.6 ± 0.8	0.54	3.1 ± 0.3	0.9 ± 0.6	79	4.2 ± 1.0	2.1 ± 2.4	21	1.84	0.95	0.00	0.62
15	MTSSL	apo	17.1 ± 0.6	0.59	3.4 ± 0.2	0.6 ± 0.4	43	4.0 ± 0.5	1.2 ± 0.3	57	1.83	0.79	0.00	0.97
15	MTSSL	Zn	21.7 ± 0.6	0.78	3.6 ± 0.2	0.7 ± 0.4	80	4.1 ± 0.8	3.1 ± 1.9	20	1.91	0.98	0.00	0.55
15	MSL	apo	12.5 ± 0.5	0.42	4.0 ± 0.3	1.5 ± 0.4	75	4.6 ± 1.1	4.9 ± 2.5	25	2.19	0.99	0.00	0.53
15	MSL	Zn	24.0 ± 2.0	0.87	4.1 ± 0.5	0.8 ± 0.7	38	4.7 ± 1.0	4.3 ± 2.4	62	1.46	0.99	0.01	0.52
37	MTSSL	apo	19.1 ± 0.9	0.67	4.8 ± 0.4	1.0 ± 1.3	23	5.5 ± 1.1	5.0 ± 1.0	77	1.61	1.12	0.00	0.23
37	MTSSL	Zn	14.4 ± 0.2	0.49	3.4 ± 0.4	2.7 ± 1.1	100				1.20		0.12	
37	MTSSL	DNA	15.4 ± 0.3	0.53	3.4 ± 0.5	3.9 ± 1.4	53	3.5 ± 0.8	1.4 ± 0.8	47	1.79	0.97	0.00	0.56
37	MSL	apo	13.8 ± 0.4	0.47	4.4 ± 0.5	4.6 ± 1.1	100				1.13		0.19	
37	MSL	Zn	17.4 ± 0.2	0.61	3.2 ± 0.2	2.1 ± 0.5	66	5.4 ± 0.4	3.9 ± 1.1	34	3.91	1.01	0.00	0.47
37	MSL	DNA	16.0 ± 0.5	0.55	3.4 ± 0.3	2.5 ± 0.5	92	6.3 ± 2.1	4.2 ± 4.2	8	1.49	0.97	0.02	0.56
37	IASL	apo	12.4 ± 1.0	0.42	4.2 ± 1.1	5.0 ± 1.1	63	4.3 ± 0.4	1.6 ± 0.8	37	1.37	1.00	0.02	0.50
37	IASL	Zn	14.8 ± 0.5	0.51	3.5 ± 0.4	3.1 ± 1.1	100				1.08		0.30	
37	IASL	DNA	13.8 ± 0.4	0.47	3.3 ± 0.5	1.3 ± 0.7	31	3.6 ± 0.4	3.4 ± 0.8	69	1.91	0.98	0.00	0.53

[a] M_D is the modulation depth, which is defined as the percentage ratio of intensity of the pure echo modulation to total echo intensity; *f* is the corresponding fraction of coupled spins in the sample, calculated by comparison to the modulation depth of calibrated sample (biradical); *r* is the center distance, *w* is the width, and % is the percentage contribution of a Gaussian population. The standard error in the population ratio depends on the boundaries in the Monte Carlo search in which the χ^2 surface is calculated. In the analysis presented here, the % contribution was determined with 10% accuracy. *F* and *P* are the statistical *F* test values comparing 1 Gaussian model to 2 Gaussians model in the fitting (subscript 1 → 2) or 2 Gaussians to 3 (2 → 3).

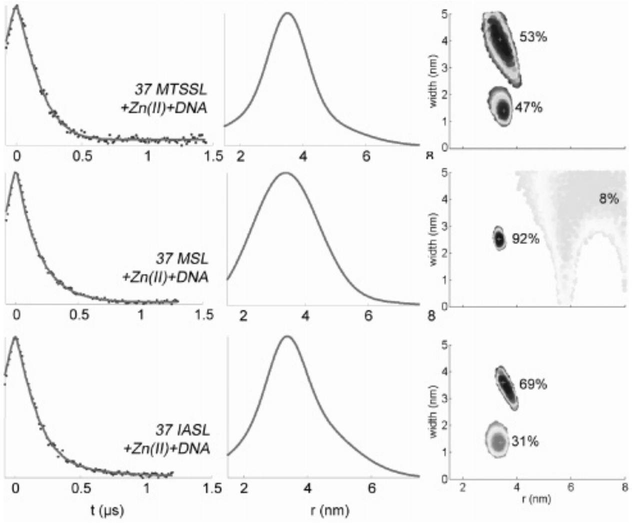

FIGURE 9: Distances between the monomers of MTSSL, MSL, and IASL spin-labeled AntR(S37C) mutants in the presence of Zn(II) and cognate DNA. Dipolar evolution (left panel, points), best fits (solid line) corresponding to distance distributions in the center panel, and χ^2 surface (right panel) are shown. The fraction of each population is displayed next to the χ^2 contours.

Modeling of Spin Label Conformations in AntR. The experimentally observed distance distributions measured by DEER for the three sites in AntR result from the convolution of spin-label motions with protein backbone motions. To disentangle this information, we modeled possible label rotamers at each site by computationally introducing the spin labels into the appropriate site in AntR, using a homology-built structure based on the MntR crystal structure (*12*). The lowest energy spin label rotamers were determined by (i) MMCM while maintaining a rigid protein structure followed by (ii) MD simulations (of 2−4 ns duration) in which all residues with atoms within a 15 Å radius of the spin label were free to move. The distance between the spin labels obtained from the MMCM calculation is plotted for each rotamer assuming a Boltzmann distribution in the energies, while the molecular dynamics distances are pooled to generate a probability density function as described in the Materials and Methods (*28*, *31*). This method is somewhat more complex and time-consuming than the free-in-a-cone rotation approach of Borbat et al. (*37*) or the rotamer library-docking approach of Jeschke et al. (*38*); however, it is likely to be more accurate as it allows for nonconventional angles.

Figure 10 compares the modeled and experimentally derived distance distributions for each spin label in all three labeled sites. There is no significant difference between the modeled and the experimental distance distributions for spin labels introduced at sites L15C and E124C, indicating that the distributions might be due to spin label rotamers and not to protein backbone heterogeneity. The differences in the experimental and modeled mean distances of the major populations of E124 are ∼0.7 nm, within the range of combined errors of the experiment (±0.3 nm) and modeling (±0.5 nm); hence, we do not consider this as significant. Computationally generated rotamers at site E124 do not account for the minor, broad components. The experimental distances for these minor populations are associated with large errors (Table 2) and thus are not well-defined. Therefore, it is not surprising that the simulations did not generate conformers that correspond to these minor experimental populations.

The 1.0 nm difference between the simulated and the experimental distances for all spin labels on site L15C is within the range of the combined experimental and modeling uncertainties (±0.5 nm, Table 2). However, the modeled distances for this site are more narrowly distributed than seen experimentally. Given that the minor broad distance distribution for this population seen in the experimental data is not well-defined, there does not appear to be a significant disagreement between modeling and experimental distributions.

Broad distance distributions are observed for site S37C in both the simulated and the experimental distances. However, the wider distributions are observed in the experimental data ($|\Delta_{model} - \Delta_{data}| \sim 1.8-3$ nm) and exceed the combined errors of the experiment (±0.5−1.1 nm) and

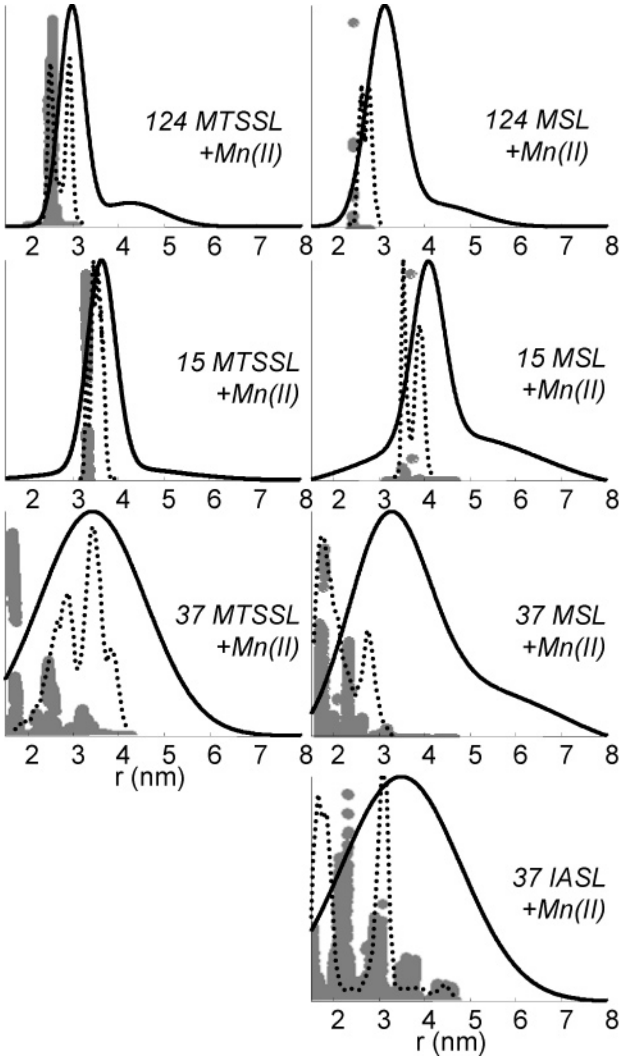

FIGURE 10: Modeled distances between the monomers of MTSSL-, MSL-, and IASL-labeled AntR mutants in the presence of metal. Experimental distance distributions (solid) are overlaid with distances from MMCM (gray points) and molecular dynamics (dotted) simulations.

modeling (±0.5 nm; *31*). Thus, in Figure 10, only the portion of the experimental distances that overlaps with the modeled distances is due to the spin label conformers. This suggests the presence of substantial backbone heterogeneity at the DNA binding region.

DISCUSSION

The conformational changes associated with metal binding in the activation of the AntR were determined by measuring side chain dynamics and the distances between equivalent positions in dimeric AntR. Our studies clearly show that the main effect of the metal binding is the restriction of side chain and backbone dynamics. This effect is most dramatic in residues found in the DNA binding region.

The activation scheme for DtxR, IdeR, and MntR has been the subject of several biochemical studies (*3*, *11*, *13*, *15*, *20*, *39*−*43*), and detailed mechanisms for activation by metal binding have been proposed. Nevertheless, structural changes associated with activation for these proteins are poorly defined. One structural scenario, disorder-to-order transition induced by metal binding and leading to dimerization, was advanced for DtxR (*14*) and more recently for IdeR (*44*). AntR, however, is already a dimer in the absence of metal (*16*), and clearly, a somewhat different mechanism for metal-induced activation is expected. One possibility is the conformational change within a monomer, another is the rearrangement of the monomers within the dimer, and a final possibility is the change of protein dynamics.

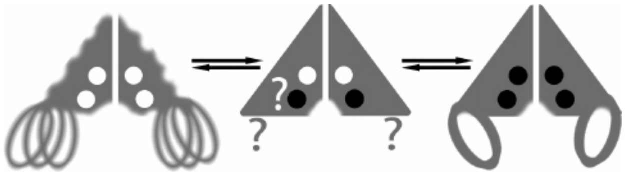

FIGURE 11: Activation mechanism of AntR. The apo dimer is dynamic with multiconformer-DNA binding site. Metal binding (black circles) induces dynamic ordering in the entire protein and brings DNA binding helices closer to each other, reducing the number of conformations that this region can adopt.

The objective of this study was to investigate the structural and dynamics changes in AntR upon activation by Zn(II) and then DNA binding. The results of this study allow us to pinpoint particular parts of AntR that are structurally and dynamically most sensitive to metal and DNA binding. Our results show that metal binding does not result in large changes in the intermonomer distances for three different points on AntR. Therefore, it is unlikely that metal binding activates AntR by rearranging the orientation or packing of monomers within the dimeric protein.

Instead, our results point to conformational changes within each monomer as providing a more plausible description for divalent metal activation. Metal binding affects the structure and dynamics primarily in the DNA binding part of AntR. The spin labels have different structures and lengths, and thus, the changes experienced by all three kinds of probes are most probably due to protein conformational change, rather than some local structural ordering that only affects the spin label conformation. Such a large change between the DNA binding helices while keeping the other two distances constant requires a structural change within the monomer. One can only speculate that bringing the DNA binding helices into proximity of each other facilitates DNA binding in a pincerlike fashion.

In a very recent study, a similar scenario for a member of the single domain family, MntR was proposed based on crystallographic results (*45*). DeWitt et al. showed that MntR has a conformational distribution of the DNA binding sites in the apo form. The positions of the helix−turn−helix motifs were distributed over a range, which was not observed in the metal-bound structure. Moreover, the DNA binding sites of MntR were further apart in the metal-free state than in the metal-bound state. These findings for MntR in crystal form are consistent with our solution data for AntR. Despite the slight differences in metal affinities (*16*, *18*) of these single domain members of the DtxR family, the activation mechanism appears to be the same.

Our data also show a decreased flexibility for all spin labels at all three sites, most probably indicating a general decrease in protein backbone motion upon activation, although we cannot exclude a possibility that all three labels are floppy on the surface protein in the apo state and somehow become rigidly attached in the presence of metal. Furthermore, close inspection of the distance distributions from DEER on the DNA binding region reveals a general trend of decreasing conformational heterogeneity as reflected in the width of distance distribution. Taken together, the data support an increase of protein order accompanying the metal binding.

Interestingly, the DNA binding did not induce any additional conformational changes over those induced by metal binding. Apparently, metal binding poised the structure of the repressor in the functionally competent state.

In light of these and previous (*16*) findings on AntR, we propose the following mechanism for repressor activation (Figure 11): The repressor exists as a dimer even in the absence of the metals. The dimer is flexible, exhibiting nanosecond backbone dynamics. Metal binding decreases protein dynamics—the protein stiffens up and brings the DNA binding regions of the two monomers in the proximity that facilitates DNA binding. DNA binding does not induce any further structural change. The activation of the AntR repressor is one of the growing examples of proteins regulated primarily by the protein dynamics in addition to conformational changes.

SUPPORTING INFORMATION AVAILABLE

EPR spectra and line shape simulations of MTSSL-, MSL-, and IASL-labeled AntR(S37C) covalently bound to DITC glass beads (Figure S1 and Table S1). This material is available free of charge via the Internet at http://pubs.acs.org.

REFERENCES

1. Tao, X., Schiering, N., Zeng, H. Y., Ringe, D., and Murphy, J. R. (1994) Iron, Dtxr, and the regulation of diphtheria-toxin expression, *Mol. Microbiol. 14*, 191−197.
2. Schmitt, M. P., Predich, M., Doukhan, L., Smith, I., and Holmes, R. K. (1995) Characterization of an iron-dependent regulatory protein (IdeR) of *Mycobacterium tuberculosis* as a functional homolog of the diphtheria toxin repressor (DtxR) from *Corynebacterium diphtheriae* [published erratum appears in (1996) *Infect. Immun. 64* (2), 681], *Infect. Immun. 63*, 4284−4289.
3. Que, Q., and Helmann, J. D. (2000) Manganese homeostasis in *Bacillus subtilis* is regulated by MntR, a bifunctional regulator related to the diphtheria toxin repressor family of proteins, *Mol. Microbiol. 35*, 1454−1468.
4. Dussurget, O., and Smith, I. (1998) Interdependence of mycobacterial iron regulation, oxidative-stress response and isoniazid resistance, *Trends Microbiol. 6*, 354−358.
5. Dussurget, O., Rodriguez, M., and Smith, I. (1996) An ideR mutant of Mycobacterium smegmatis has derepressed siderophore production and an altered oxidative-stress response, *Mol. Microbiol. 22*, 535−544.
6. Tao, X., Boyd, J., and Murphy, J. R. (1992) Specific binding of the diphtheria tox regulatory element dtxr to the tox operator requires divalent heavy-metal ions and a 9-base-pair interrupted palindromic sequence, *Proc. Natl. Acad. Sci. U.S.A. 89*, 5897−5901.
7. Schiering, N., Tao, X., Zeng, H. Y., Murphy, J. R., Petsko, G. A., and Ringe, D. (1995) Structures of the apo-activated and the metal ion-activated forms of the diphtheria tox repressor from corynebacterium-diphtheriae, *Proc. Natl. Acad. Sci. U.S.A. 92*, 9843−9850.
8. Feese, M. D., Ingason, B. P., Goranson-Siekierke, J., Holmes, R. K., and Hol, W. G. J. (2001) Crystal structure of the iron-dependent regulator from *Mycobacterium tuberculosis* at 2.0-angstrom resolution reveals the Src homology domain 3-like fold and metal binding function of the third domain, *J. Biol. Chem. 276*, 5959−5966.
9. Wisedchaisri, G., Holmes, R. K., and Hol, W. G. J. (2004) Crystal structure of an IdeR-DNA complex reveals a conformational change in activated IdeR for base-specific interactions, *J. Mol. Biol. 342*, 1155−1169.
10. Wylie, G. P., Rangachari, V., Bienkiewicz, E., and Logan, T. M. (2003) Structure and thermodynamics of SH3-like C-terminal domain of Diphtheria toxin repressor (DtxR) binding to proline-rich linker: Understanding the role of SH3 domain in activation, *Biophys. J. 84*, 505A−505A.
11. Golynskiy, M. V., Davis, T. C., Helmann, J. D., and Cohen, S. M. (2005) Metal-induced structural organization and stabilization of the metalloregulatory protein MntR, *Biochemistry 44*, 3380−3389.
12. Glasfeld, A., Guedon, E., Helmann, J. D., and Brennan, R. G. (2003) Structure of the manganese-bound manganese transport regulator of *Bacillus subtilis*, *Nat. Struct. Biol. 10*, 652−657.
13. Tao, X., Zeng, H. Y., and Murphy, J. R. (1995) Transition-metal ion activation of DNA-binding by the diphtheria tox repressor requires the formation of stable homodimers, *Proc. Natl. Acad. Sci. U.S.A. 92*, 6803−6807.
14. Twigg, P. D., Parthasarathy, G., Guerrero, L., Logan, T. M., and Caspar, D. L. D. (2001) Disordered to ordered folding in the regulation of diphtheria toxin repressor activity, *Proc. Natl. Acad. Sci. U.S.A. 98*, 11259−11264.
15. Lieser, S. A., Davis, T. C., Helmann, J. D., and Cohen, S. M. (2003) DNA-binding and oligomerization studies of the manganese(II) metalloregulatory protein MntR from *Bacillus subtilis*, *Biochemistry 42*, 12634−12642.
16. Sen, K. I., Sienkiewicz, A., Love, J. F., vanderSpek, J. C., Fajer, P. G., and Logan, T. M. (2006) Mn(II) binding by the anthracis repressor from *Bacillus anthracis*, *Biochemistry 45*, 4295−4303.
17. Kliegman, J. I., Griner, S. L., Helmann, J. D., Brennan, R. G., and Glasfeld, A. (2006) Structural basis for the metal-selective activation of the manganese transport regulator of *Bacillus subtilis*, *Biochemistry 45*, 3493−3505.
18. Golynskiy, M. V., Gunderson, W. A., Hendrich, M. P., and Cohen, S. M. (2006) Metal binding studies and EPR spectroscopy of the manganese transport regulator MntR, *Biochemistry 45*, 15359−15372.
19. Altenbach, C., Flitsch, S. L., Khorana, H. G., and Hubbell, W. L. (1989) Structural studies on transmembrane proteins. 2. Spin labeling of bacteriorhodopsin mutants at unique cysteines, *Biochemistry 28*, 7806−7812.
20. Love, J. F. (2003) Department of Microbiology, Boston University School of Medicine, Boston, MA.
21. Fajer, P. G., Bennett, R. L. H., Polnaszek, C. F., Fajer, E. A., and Thomas, D. D. (1990) General-method for multiparameter fitting of high-resolution EPR-spectra using a simplex algorithm, *J. Magn. Reson. 88*, 111−125.
22. Adhikari, B. B., Somerset, J., Stull, J. T., and Fajer, P. G. (1999) Dynamic modulation of the regulatory domain of myosin heads by pH, ionic strength, and RLC phosphorylation in synthetic myosin filaments, *Biochemistry 38*, 3127−3132.
23. Baumann, B. A. J., Hambly, B. D., Hideg, K., and Fajer, P. G. (2001) The regulatory domain of the myosin head behaves as a rigid lever, *Biochemistry 40*, 7868−7873.
24. Li, H. C., and Fajer, P. G. (1994) Orientational changes of troponin-C associated with thin filament activation, *Biochemistry 33*, 14324−14332.
25. Szczesna, D., and Fajer, P. G. (1995) The tropomyosin domain is flexible and disordered in reconstituted thin-filaments, *Biochemistry 34*, 3614−3620.
26. Fajer, P. G., Gyimesi, M., Malnasi-Csizmadia, A., Bagshaw, C., Sen, K. I., and Song, L. (2007) Myosin cleft closure by DEER and dipolar EPR, *J. Phys.: Condens. Matter 19*, 285208−285217.
27. Brooks, B. R., Bruccoleri, R. E., Olafson, B. D., States, D. J., Swaminathan, S., and Karplus, M. (1983) Charmm—A program for macromolecular energy, minimization, and dynamics calculations, *J. Comput. Chem. 4*, 187−217.
28. Fajer, M., Fajer, P. G., and Sale, K. L. (2007) Molecular modeling of spin labels, in *ESR Spectroscopy in Membrane Biophysics* (Hemminga, M., and Berliner, L., Eds.) Vol. 27, pp 254−260, Springer-Verlag, New York.
29. Lambert, C., Leonard, N., De Bolle, X., and Depiereux, E. (2002) ESyPred3D: Prediction of proteins 3D structures, *Bioinformatics 18*, 1250−1256.
30. Sale, K., Sar, C., Sharp, K. A., Hideg, K., and Fajer, P. G. (2002) Structural determination of spin label immobilization and orientation: A Monte Carlo minimization approach, *J. Magn. Reson. 156*, 104−112.

31. Sale, K., Song, L. K., Liu, Y. S., Perozo, E., and Fajer, P. (2005) Explicit treatment of spin labels in modeling of distance constraints from dipolar EPR and DEER, *J. Am. Chem. Soc. 127*, 9334−9335.
32. Metropolis, N., Rosenbluth, A. W., Rosenbluth, M. N., Teller, A. H., and Teller, E. (1953) Equation of state calculations by fast computing machines, *J. Chem. Phys. 21*, 1087−1092.
33. Humphrey, W., Dalke, A., and Schulten, K. (1996) VMD: Visual molecular dynamics, *J. Mol. Graphics 14*, 33.
34. Fajer, P. G. (2000) Electron spin resonance spectroscopy labeling in peptide and protein analysis. In *Encyclopedia of Analytical Chemistry* (Meyers, R. A., Ed.) pp 5725−5761, John Wiley & Sons Ltd., Chichester.
35. Rabenstein, M. D., and Shin, Y. K. (1995) Determination of the distance between 2 spin labels attached to a macromolecule, *Proc. Natl. Acad. Sci. U.S.A. 92*, 8239−8243.
36. Pannier, M., Veit, S., Godt, A., Jeschke, G., and Spiess, H. W. (2000) Dead-time free measurement of dipole-dipole interactions between electron spins, *J. Magn. Reson. 142*, 331−340.
37. Borbat, P. P., McHaourab, H. S., and Freed, J. H. (2002) Protein structure determination using long-distance constraints from double-quantum coherence ESR: Study of T4 lysozyme, *J. Am. Chem. Soc. 124*, 5304−5314.
38. Jeschke, G., and Polyhach, Y. (2007) Distance measurements on spin-labelled biomacromolecules by pulsed electron paramagnetic resonance, *Phys. Chem. Chem. Phys. 9*, 1895−1910.
39. Manabe, Y. C., Hatem, C. L., Kesavan, A. K., Durack, J., and Murphy, J. R. (2005) Both *Corynebacterium diphtheriae* DtxR-(E175K) and *Mycobacterium tuberculosis* IdeR(D177K) are dominant positive repressors of IdeR-regulated genes in *M. tuberculosis*, *Infect. Immun. 73*, 5988−5994.
40. Marin, V., Semavina, M., Sen, K. I., Love, J. F., Guerrero, L. R., Caspar, D. L. D., Murphy, J. R., and Logan, T. M. (2003) Interdomain interactions are required for repressor function in diphtheria toxin repressor, *Biophys. J. 84*, 496A−496A.
41. Rangachari, V., Guerrero, L., Bienkienwicz, E. A., Love, J. F., Murphy, J., and Logan, T. M. (2004) Sequence of metal binding and conformational ordering leading to diphtheria toxin repressor (DtxR) activation, *Biophys. J. 86*, 617A−617A.
42. Spiering, M. M., Ringer, D., Murphy, J. R., and Marletta, M. A. (2003) Metal stoichiometry and functional studies of the diphtheria toxin repressor, *Proc. Natl. Acad. Sci. U.S.A. 100*, 3808−3813.
43. Schmitt, M. P. (2002) Analysis of a DtxR-like metalloregulatory protein, MntR, from *Corynebacterium diphtheriae* that controls expression of an ABC metal transporter by an Mn2+-dependent mechanism, *J. Bacteriol. 184*, 6882−6892.
44. Semavina, M., Beckett, D., and Logan, T. M. (2006) Metal-linked dimerization in the iron-dependent regulator from *Mycobacterium tuberculosis*, *Biochemistry 45*, 12480−12490.
45. DeWitt, M. A., Kliegman, J. I., Helmann, J. D., Brennan, R. G., Farrens, D. L., and Glasfeld, A. (2007) The conformations of the manganese transport regulator of *Bacillus subtilis* in its metal-free state, *J. Mol. Biol. 365*, 1257−1265.

BI700859P